

RESEARCH ARTICLE

10.1002/2014JD021787

Key Points:

- Meteor radar echo decay times are reduced at low altitudes
- Three-body attachment of positive ions shortens meteor echo decay times
- Attachment effects exceed diffusion at a constant atmospheric density

Supporting Information:

- Simulation S1

Correspondence to:

J. P. Younger,
joel.younger@adelaide.edu.au

Citation:

Younger, J. P., C. S. Lee, I. M. Reid, R. A. Vincent, Y. H. Kim, and D. J. Murphy (2014), The effects of deionization processes on meteor radar diffusion coefficients below 90 km, *J. Geophys. Res. Atmos.*, 119, 10,027–10,043, doi:10.1002/2014JD021787.

Received 24 MAR 2014

Accepted 5 AUG 2014

Accepted article online 11 AUG 2014

Published online 22 AUG 2014

The effects of deionization processes on meteor radar diffusion coefficients below 90 km

J. P. Younger^{1,2}, C. S. Lee³, I. M. Reid^{1,2}, R. A. Vincent², Y. H. Kim⁴, and D. J. Murphy⁵
¹ATRAD Pty. Ltd., Thebarton, South Australia, Australia, ²School of Chemistry and Physics, University of Adelaide, Adelaide, South Australia, Australia, ³Korea Polar Research Institute, Incheon, Republic of Korea, ⁴Department of Astronomy and Space Science, Chungnam National University, Daejeon, Republic of Korea, ⁵Australian Antarctic Division, Kingston, Tasmania, Australia

Abstract The decay times of VHF radar echoes from underdense meteor trails are reduced in the lower portions of the meteor region. This is a result of plasma neutralization initiated by the attachment of positive trail ions to neutral atmospheric molecules. Decreased echo decay times cause meteor radars to produce erroneously high estimates of the ambipolar diffusion coefficient at heights below 90 km, which affects temperature estimation techniques. Comparisons between colocated radars and satellite observations show that meteor radar estimates of diffusion coefficients are not consistent with estimates from the Aura Microwave Limb Sounder satellite instrument and that colocated radars operating at different frequencies estimate different values of the ambipolar diffusion coefficient for simultaneous detections of the same meteors. Loss of free electrons from meteor trails due to attachment to aerosols and chemical processes were numerically simulated and compared with observations to determine the specific mechanism responsible for low-altitude meteor trail plasma neutralization. It is shown that three-body attachment of positive metal ions significantly reduces meteor radar echo decay times at low altitudes compared to the case of diffusion only that atmospheric ozone plays little part in the evolution of low-altitude underdense meteor trails and that the effect of three-body attachment begins to exceed diffusion in echo decay times at a constant density surface.

1. Introduction

Estimates of the ambipolar diffusion coefficient inferred from underdense meteor trail radar echo decay times vary depending on the radar frequency and show disagreement with other measurement techniques. As meteor radar diffusion coefficients provide the basis for temperature measurement techniques in the 80–100 km height range [see, e.g., *Hocking, 1999; Cervera and Reid, 2000*], it is vital to understand what causes meteor radar echo decay times to deviate from the predictions of established theory. A detailed analysis of the physical processes involved in the evolution of meteor plasma provides clues as to the mechanisms responsible for the differences between observations and predictions of established theory.

Meteor trails are narrow columns of plasma that are the result of bodies undergoing ablation during atmospheric entry. Meteoroids enter the atmosphere at speeds in excess of the terrestrial escape velocity of 11.2 km s^{−1}. Collisions with atmospheric atoms and molecules remove small amounts of meteoric material through sputtering [*Rogers et al., 2005*] and convert a portion of the meteoroid's kinetic energy into thermal energy. For meteors larger than about 50 μm in diameter, this results in heating to temperatures at which material rapidly evaporates from the surface of the meteoroid [*Love and Brownlee, 1991*]. Sputtered and evaporated meteoric material is ionized by subsequent collisions with atmospheric atoms and molecules, resulting in a column of plasma behind the meteoroid.

Meteoric ions are rapidly brought into thermal equilibrium with the surrounding atmosphere via further collisions, producing an approximately Gaussian radial distribution of plasma density about the meteor trail axis, with initial radius r_0 [*Jones, 1995*]. Following the formation of the trail, the development of the plasma density distribution is governed by ambipolar diffusion [*Herlofson, 1947*]. The quasi-neutrality condition dictates that any appreciable charge separation is suppressed by the resultant electric field. Given the much greater mass of ions relative to electrons, the diffusive motion of the plasma away from the trail axis is

dominated by the motion of the ions in the trail. Thus, the rate of change of electron density, $n_e(r, t)$, at a distance r from the trail axis and time t since formation is given by

$$\frac{\partial n_e}{\partial t} = \frac{D}{r} \frac{\partial}{\partial r} \left(r \frac{\partial n_i}{\partial r} \right), \quad (1)$$

where D is the ambipolar diffusion coefficient of meteoric ions the atmosphere and $n_i = n_e$ is the positive ion density [McKinley, 1961].

If the density of a meteor trail is sufficiently low that the dielectric constant is positive everywhere in the trail, the meteor trail is classed as underdense. This transition occurs around a meteor trail density of $2.4 \times 10^{14} \text{ el m}^{-3}$ [McKinley, 1961]. Radio waves undergo volume scatter throughout underdense meteor trails and produce specular, coherent echoes. For the case of monostatic radar, specular echoes are produced when the trail is perpendicular to the line of sight to the radar. The passage of a meteoroid across the field of view of a radar followed by an underdense trail results in a knife-edge type diffraction pattern at the receiver. The observed echo exhibits Fresnel oscillations over time due to interference between the backscatter from different segments along the length of the trail.

The Fresnel diffraction pattern is modulated by a decay in observed echo power over time due to the radial expansion of the trail. The observed backscatter amplitude, A , at time t is given by the proportional relation

$$A \propto 2\pi \int_0^\infty n_e(r, t) r J_0 \left(\frac{4\pi r}{\lambda} \right) dr, \quad (2)$$

where r is the distance from the trail axis, J_0 is a zeroth-order Bessel function and λ is wavelength of the radar [McKinley, 1961]. J_0 is a periodic function with respect to radius, which is positive directly adjacent the trail axis. As electrons move away from the trail axis, the central positive contribution to echo amplitude decreases. Additionally, the increase in electron density in negative regions produces greater negative backscatter amplitude, which interferes destructively with scatter from near the trail axis.

Herlofson [1947] showed that the diffusion of ionized material away from the trail axis produces an exponential decay in echo strength over time, with the time taken for the observed echo to decay from the initial peak power by a factor of e^{-1} is given by

$$\tau = \frac{\lambda^2}{16\pi^2 D}. \quad (3)$$

Furthermore, Jones [1995] demonstrated that the exponential echo decay occurs for any radially symmetric initial distribution of meteoric plasma. Thus, the ambipolar diffusion coefficient may be inferred from the decay times of underdense meteor echoes.

The decay time of radar echoes from underdense meteor trails has long been used to produce estimates of the ambipolar diffusion coefficient of the atmosphere in the meteor region at heights around 80–100 km [Hocking, 2011]. The ambipolar diffusion coefficient is of particular interest to atmospheric studies, as it is a function of temperature and pressure, as given by

$$D = 6.39 \times 10^{-2} K_0 \frac{T^2}{p} = 2.23 \times 10^{-4} K_0 \frac{T}{\rho}, \quad (4)$$

where K_0 is the zero field mobility of the diffusing ions [Mason and McDaniel, 1988], T is the temperature of the atmosphere, p is pressure, and ρ is atmospheric density. Thus, estimates of D can be used to infer the temperature of the atmosphere in the meteor region by supplying a known value of pressure (pressure climatology method [Tsutsumi et al., 1994; also see, e.g., Cervera and Reid, 2000]) or by analysis of the gradient of $\log D$ with respect to height (gradient method [Hocking, 1999]).

2. Instrumentation

VHF meteor radars have become a common tool around the world for the measurement of mesospheric winds and estimates of the ambipolar diffusion coefficient [Baggaley, 2009]. The most common design, described by Jones et al. [1998], consists of a single transmit antenna and an array of five receive antennas. The receive antennas are arranged in two perpendicular interferometric baselines to estimate the angle of arrival of incident backscatter from meteor trails. Each baseline consists of two antenna pairs, separated at

spacings of 2.0 and 2.5 times the radar wavelength. By combining the phase differences across different pairs of antennas, the direction to a received echo can be unambiguously determined [Holdsworth, 2005].

Two ATRAD meteor radars, both located at Davis Station, Antarctica (68.6°S, 78.0°E), are the focus of this study. A dedicated 33 MHz (9.1 m) meteor radar is colocated with a hybrid 55 MHz (5.5 m) Stratospheric-Tropospheric (ST)/meteor radar system [Holdsworth *et al.*, 2008]. The 55 MHz system shares a single-transceiver unit between antenna arrays for the ST and meteor system [Reid *et al.*, 2006]. This reduces the available time for meteor observations during summer months when the ST system is operating, with observation periods typically allocated equally between the ST and meteor modes. Both transmit a 3.6 km long, 4 bit complimentary coded pulse with a pulse repetition frequency of 430 Hz. Underdense meteors are recognized by searching for nonoscillatory echoes in the 70–110 km height range with a sharp initial rise and characteristic exponential decay following peak amplitude [Holdsworth *et al.*, 2004].

Meteor detections used in the analysis are restricted to zenith angles of less than 45° to reduce uncertainty in detection heights. This criterion results in a height estimate uncertainty of less than ± 1 km, given the meteor radar range resolution of 1.8 km [Holdsworth *et al.*, 2008].

Independent measurements of atmospheric state were obtained from the Aura MLS (Microwave Limb Sounder) instrument [Waters *et al.*, 2006]. Launched in 2004, the MLS instrument aboard the Aura EOS satellite measures microwave emissions across five bands ranging from 118 GHz to 2.5 THz. Data products include the density of a number of different atmospheric species, neutral temperature, and geopotential height. Observations are made every 165 km along the orbital track, producing vertical profiles of each parameter gridded on fixed pressure surfaces.

Aura MLS data were used to calculate diffusion coefficients for comparison with meteor radar observations using equation (4). A value of $K_0 = 2.5 \times 10^{-4} \text{ m}^2 \text{ s}^{-1} \text{ V}^{-1}$ was chosen as representative of ions present in meteor trails [see, e.g., Cervera and Reid, 2000]. Geometric heights, z for Aura MLS observations were computed from geopotential heights, z_g via the equation $z = z_g R_e(\phi) [R_e(\phi) - z_g]^{-1}$, where $R_e(\phi)$ is the radius of Earth at latitude ϕ , based on the WGS84 ellipsoid [Decker, 1986]. Atmospheric densities were calculated using the ideal gas law $\rho = p (R_s T)^{-1}$, where $R_s = 287.058$ is the specific gas constant of dry air. Satellite observations were restricted to within a 200 km radius of Davis Station, which provided a compromise between collocation of meteor radar/MLS data and frequency of MLS measurements. Temporal differences between the radars and satellite data were minimized by only considering meteor detections within ± 2 hours of each satellite observation. The size of this time bin ensured sufficient meteor detections for comparison with MLS measurements, while avoiding excessive variation due to diurnal and semidiurnal tides.

3. Observational Discrepancies

The diffusion coefficient estimates from the two colocated radars at Davis Stations were compared with each other, as well as to diffusion coefficients calculated from Aura MLS satellite observations of temperature and geopotential height. While the decay time, τ , is the parameter being directly measured by the meteor radars, the value of D calculated using equation (3) was chosen for comparisons, as the true value is independent of radar wavelength.

The observations allow us to define three types of deviation between observations: offset, gradient difference, and height of gradient reversal (turnaround height). Offset describes the absolute difference between different estimates of the diffusion coefficient and gradient describes the difference in the slope of $\log D$ with respect to height for the profiles from different sources. An offset in the diffusion coefficient will produce errors in temperatures derived from diffusion coefficients using the climatology method, while errors in the slope of $\log D$ will affect temperatures obtained from the gradient method put forward by Hocking [1999].

The gradient reversal phenomena are seen at low altitudes in meteor radar diffusion coefficient profiles [Kim *et al.*, 2010]. Given the inverse dependence of D on atmospheric density, $\log D$ should be an approximately linear function of geometric height throughout the meteor detection region. What is observed, however, is that below some critical atmospheric density the slope of $\log D$ reverses sign, resulting in an apparent increase in the diffusion coefficient estimate with decreasing height [Lee *et al.*, 2013].

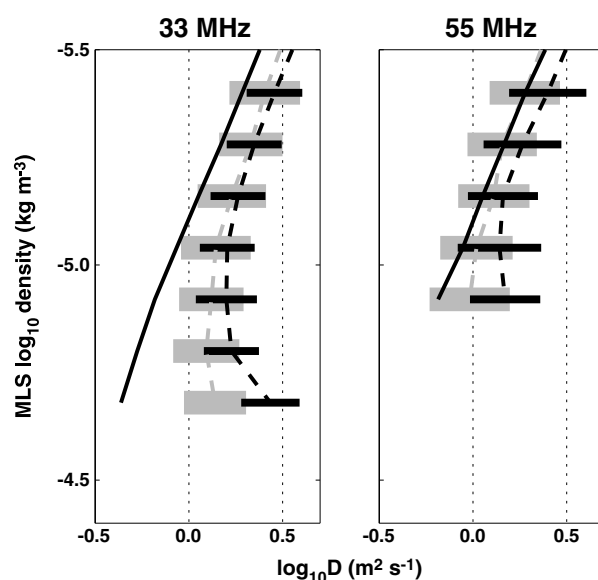


Figure 1. Diffusion coefficient estimates as a function of Aura MLS atmospheric density for January, 2009. Solid: Aura MLS diffusion coefficients. Light gray dashed: weakest 50% of meteors. Black dashed: strongest 50% of meteors. Error bars indicate 1 standard deviation. Calculated using 2973 detections for 55 MHz and 29,082 detections for 33 MHz, both observed within ± 2 h of MLS observations.

The diffusion coefficient profiles in Figure 1 demonstrate the different types of discrepancies seen in meteor radar diffusion coefficient estimates. In this example, meteor detections have been separated into strong and weak trails on the basis of uncalibrated electron density. Using the meteor radar response function [see, e.g., *Cepelcha et al.*, 1998], a relative measure of electron line density, q , can be made from uncalibrated echo power, P_R , using the relation $q \propto (P_R R^3 \lambda^{-3})^{1/2}$, where R is the distance between the trail and radar. Weak and strong detections for the profiles in Figure 1 were classified as those below and above the median uncalibrated q , respectively.

While the diffusion coefficients obtained from the lowest density quartile of meteor trails detected by the 55 MHz radar are in good agreement with MLS at and above the peak detection height, 55 MHz detections from more dense meteor trails and all 33 MHz detections exhibits significant offset from the MLS-derived value of D . This

is especially pronounced at lower altitudes, where an unrealistically large increase in temperature would be required to explain the substantial increase in the estimate of the diffusion coefficient. Furthermore, both meteor radars display a dependence of the diffusion coefficient estimate on q .

The difference between diffusion coefficient estimates of the two radars is not immediately clear in Figure 1. In order to compare the diffusion coefficients estimates of the two radars, data from 2009 were analyzed to find simultaneous detections by both systems. Using spatial-temporal bins of 3° azimuth, 3° zenith, and 1 min, detections from each radar were compared to find matches, with bins containing more than one detection for a single radar discarded to avoid ambiguity. With these criteria, it was found that 224,971 meteors were detected simultaneously by both radars during 2009. Restriction of detections to less than 45° zenith

angle further reduced this number to 63,736 detections available for direct comparison between the two radars.

The comparison of the diffusion coefficient estimates from the two radars, shown in Figure 2, clearly shows that the 33 MHz radar systematically produces higher values for D than the 55 MHz radar. This indicates that the assumption of purely exponential echo decay necessary for equation (3) does not hold up under close scrutiny, at least for 33 MHz detections. As *Jones* [1995] showed that linear diffusion and hence, exponential echo decay, is independent of the shape of the initial distribution of meteoric plasma about the trail axis, an additional factor must be affecting the evolution of plasma in meteor trails. While some of the

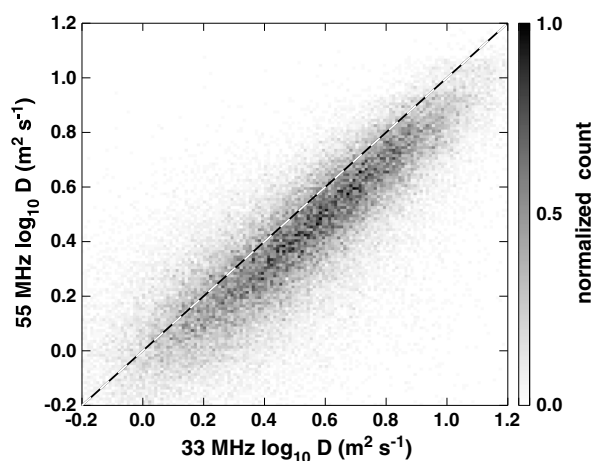


Figure 2. Comparison of diffusion coefficients estimates for 63,736 meteors detected simultaneously by both 33 and 55 MHz radars at Davis Station, Antarctica during 2009. The dashed line indicates exact agreement.

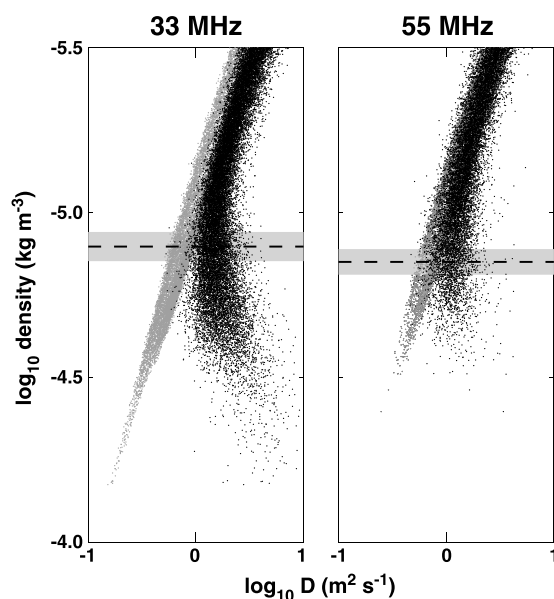


Figure 3. Simultaneous estimates of the ambipolar diffusion coefficient for 2007–2009 at Davis Station, Antarctica from Aura MLS satellite observations (gray points) and meteor radars (black points). The dashed line indicates the center of a quadratic fit to $\log_{10} D$ as a function of atmospheric density as measured by MLS. The shaded horizontal band indicates the uncertainty in the center of the fitted curve.

discrepancy may be due to the choice of K_0 used to calculate D from MLS data, the range of possible values of K_0 is not sufficient to produce the observed offset from MLS values of D .

This analysis illustrates the behavior of the difference between meteor radar and MLS measurements as a function of atmospheric density. It can be seen in Figure 3 that, at heights above the turnaround height, the difference between meteor radar and MLS values of $\log D$ settles to an approximately constant value. While the absolute error in the diffusion coefficient can be substantial, the gradient of the diffusion coefficient profile is relatively unaffected. This is encouraging with regard to the gradient method of temperature estimation, which relies on the slope of $\log D$ with respect to height around the height of maximum meteor detections. For the radars considered, this height varies between 87 and 90 km.

A comparison between meteor radar diffusion coefficient turnaround and neutral atmospheric density reveals that the gradient

reversal of meteor radar $\log D$ estimates occurs at a well-defined density for each radar, as shown in Figure 3. The critical density was determined by fitting a second-order polynomial to $\log D$ as a function of $\log \rho$ for both radars, using data from 2007 to 2009. It was found that the 33 and 55 MHz meteor radars exhibited turnaround at $\log_{10} \rho = -4.90 \pm 0.04$ and -4.85 ± 0.04 , respectively.

A comparison of the deviation between meteor radar and MLS satellite data over the course of 3 years is shown in Figure 4. This shows that the general behavior of the deviation between meteor radar and MLS values of D does not change with respect to time, save for an increase in the offset at all heights in summer. The height of the atmospheric density at which meteor radar estimates of $\partial \log D / \partial z$ change sign in Figure 3 is

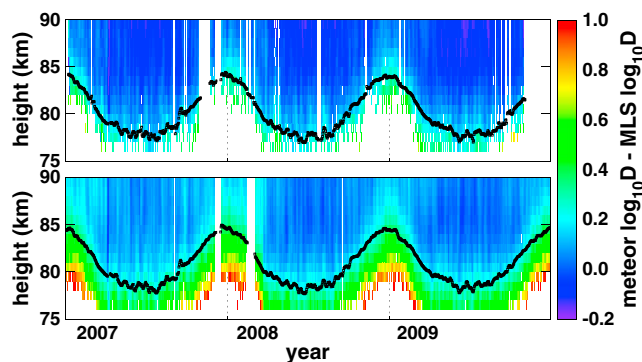


Figure 4. Difference between diffusion coefficient estimates from the Davis Station meteor radars and Aura MLS satellite instrument for the period 1 January 2007 to 31 December 2009. (top) 55 MHz. (bottom) 33 MHz. Black boxes show the heights of the turnaround density level for each frequency from Figure 3, as measured by MLS. Data have been smoothed using a 5 day running mean. Dashed vertical lines denote 1 January for each year. White spaces indicate missing data.

plotted over the data in Figure 4 and closely follows the height below which the deviation between diffusion coefficient estimates suddenly increases. It can also be seen that the gradient of the diffusion coefficient profiles agrees well between radar and satellite data, as evidenced by the constant value of $\Delta \log D$ above the turnaround height for any given day.

In terms of the impact on temperature estimates, the difference between the two radars of $\Delta \log_{10} D \approx 0.1$ near peak detection height corresponds to a 12% difference to the temperature estimates made using the pressure climatology method. At lower altitudes, where the reversal of the gradient of $\log D$ estimates produces large offsets,

temperature estimates made using the pressure climatology method may differ from MLS values by more than a factor of 3.

Meek et al. [2013] found a seasonal dependence of the deviation between MLS and meteor radar temperature gradients, which were complemented by increased deviation between MLS temperatures and meteor radar temperatures obtained using the pressure climatology method. It is important to note, however, that the analysis of *Meek et al.* [2013] focused on fixed geometric heights, while Figures 1, 3, and 4 all demonstrate the importance of atmospheric density. It is likely that some component of the error seen by *Meek et al.* [2013] is due to seasonal height fluctuations of atmospheric density contours moving areas of anomalous diffusion across the analysis zone.

The observations show that the deviations from diffusion-only theory affecting meteor radar diffusion coefficient estimates are the absolute error in D and the turnaround of $\log D$ at low altitudes. These effects occur at all times of the year with the height of meteor radar $\log D$ gradient reversal closely correlated to a constant atmospheric density surface. The gradient of $\log D$ is relatively unaffected above the turnaround height, despite the significant offset in the estimated value of $\log D$.

4. Aerosol Attachment

One mechanism that has been considered for the alteration of meteor radar echo decay times is the absorption of free electrons in meteor trails by aerosols [*Havnes and Sigernes*, 2005]. Modeling of meteor trail electron attachment to aerosols [*Younger et al.*, 2008] shows that aerosols may have an effect on meteor radar echo decay times under certain circumstances, but the substantial discrepancies seen in low-altitude observations are well beyond what may be expected from aerosol attachment. In order to remove aerosol attachment from consideration as a primary mechanism for free electron loss in meteor trails, a more thorough examination of the process was conducted.

Small particles are present in the mesosphere as a result of meteoric ablation and the formation of ice crystals at low temperatures. Electrons may be lost by attachment to the surface of aerosol particles, resulting in changes to the observed echo power from the distortion of the electron density distribution of meteor trails. In the presence of absorbing aerosols, equation (1) becomes

$$\frac{\partial n_e}{\partial t} = \frac{D}{r} \frac{\partial}{\partial r} \left(r \frac{\partial n_e}{\partial r} \right) - R_{ed} n_d n_e, \quad (5)$$

where R_{ed} is the attachment rate of free electrons to aerosol particles and n_d is the aerosol density.

Meteors are responsible for two types of mesospheric dust particles with diameters of less than 10 nm. Interplanetary dust particles (IDP) are the result of incident meteoroids that are too small to be heated to evaporative temperature, due to their high cross section to volume ratio. IDPs form a population of particles that have undergone partial or no melting. Meteoric smoke particles (MSP) are formed by the condensation of evaporated meteoric material [*Kalashnikova et al.*, 2000; *Plane*, 2012].

Ice crystals with diameters of up to 60 nm [*Lübken and Rapp*, 2001] can form in the mesosphere when temperatures drop below the sublimation point. The low temperatures necessary for ice crystal formation only occur near the mesopause in polar regions during summer months, when the mesosphere is coldest [*Cho and Röttger*, 1997]. The presence of ice crystals, which are thought to nucleate on MSPs, is responsible for the noctilucent cloud phenomenon, which has in turn been associated with observations of increased radar backscatter known as polar mesospheric summer echoes (PMSE) [*Klekociuk et al.*, 2008].

Two factors determine the importance of aerosol absorption of electrons on the development of meteor trails: the density of absorbing aerosols, n_d , and the electron capture rate, R_{ed} . Dynamical models have predicted MSP densities as high as 10^{10} m^{-3} [*Megner et al.*, 2006], although rocket observations have observed densities of about 10^9 m^{-3} [*Amyx et al.*, 2008]. It should be noted that aerosols are not uniformly distributed but occur primarily in a 5–10 km wide layer at heights between 75 and 95 km. The electron capture rate is a function of aerosol particle charge and radius as described by *Rapp* [2000], with values of about $R_{ed} = 10^{-8} - 10^{-10} \text{ m}^3 \text{ s}^{-1}$.

Aerosol absorption differs from conventional attachment and recombination processes in that the mass of aerosol particles is substantially greater than ions in the trail. This makes the position of aerosol particles

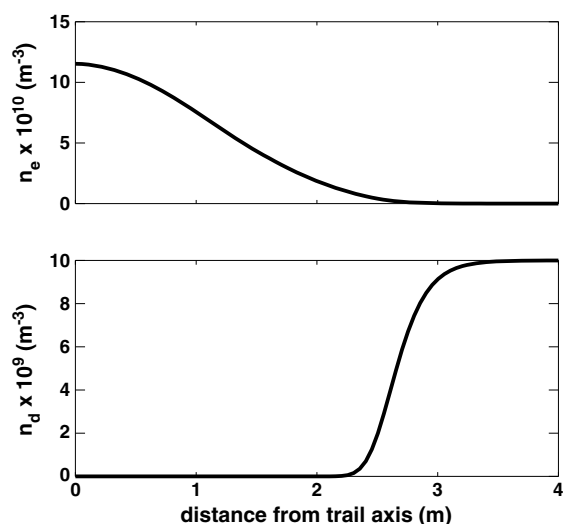


Figure 5. Numerical prediction of the densities of (top) free electrons and (bottom) absorbing aerosols after echo amplitude has decayed by a factor of e^{-2} . Model parameters: $q = 10^{12} \text{ m}^{-1}$, $r_0 = 1 \text{ m}$, $D = 2 \text{ m}^2 \text{ s}^{-1}$, $R_{ed} = 10^{-8} \text{ m}^3 \text{ s}^{-1}$, and $\lambda = 5.5 \text{ m}$.

and time. It is important to note, however, that all radars used in that study had frequencies between 32.5 and 35.3 MHz. The profiles presented also clearly exhibit turnaround behavior at low altitudes, which was not discussed.

Younger *et al.* [2008] extended the modeling of Havnes and Sigernes [2005], taking into account the effects of absorber depletion over time and analyzing the observed effects at radar wavelengths of 33 and 55 MHz. The results indicated that the decay time effects of aerosol absorption are dependent on the wavelength of the radar, with the possibility of extended echo decay times under some conditions. The counterintuitive scenario of electron loss resulting in longer echo decay times will result in lower values of the derived diffusion coefficient estimate.

4.1. Aerosol Numerical Model

An improved version of the numerical model from Younger *et al.* [2008] was constructed to investigate the possible effects of aerosol-electron attachment on decay times for a range of radar wavelengths, trail electron line densities, and aerosol conditions. Electron density, n_e , and aerosol dust density, n_d , were solved simultaneously by applying the fourth-order Runge-Kutta method to equation (5) and $\partial n_d / \partial t = R_{ed} n_e n_d$. A time step of 10^{-5} s was used with a 10 m spatial domain of 200 points separated by 0.05 m, with an initial trail radius of 1 m. The diffusion and absorption of meteor trail electrons were calculated at each step and the backscattered amplitude of the radar echo was calculated using equation (2). The predicted decay time was determined by the time taken for the echo power to be reduced to a factor of $\exp(-1)$ of the original value.

During absorption of meteor trail electrons by aerosols, the density of available absorbers is rapidly depleted at the center of the trail, which can be seen in Figure 5. Following the rapid saturation of absorbing aerosols near the center of the trail, diffusion becomes the dominant mechanism for the reduction of electron density near the center of the trail and the absorption process gradually moves further from the trail axis.

The effect of the loss of trail electrons to aerosol attachment is dependent on the radial distance from the trail axis at which absorption occurs, as compared to the Bessel weighting function in equation (2). As described by Younger *et al.* [2008] the loss of scattering electrons from positive regions of $rJ_0(4\pi r/\lambda)$ will reduce echo amplitude, while the loss of scattering electrons from regions with negative values of $rJ_0(4\pi r/\lambda)$ will remove destructive interference, adding to echo amplitude. Thus, the effect of electron loss to aerosols is strongly dependent on the wavelength of the observing radar.

An example of the predicted reduction to decay times is shown in Figure 6 for the strong absorption limiting case of $R_{ed} = 10^{-8} \text{ m}^3 \text{ s}^{-1}$ and $n_d = 10^{10} \text{ m}^{-3}$. For trails with low electron line densities, aerosol

effectively static over the time scales involved in underdense meteor echo decay. The result of the attachment of an electron to an aerosol particle is that the charge becomes fixed in space. Under the condition of quasi-neutrality, the motion of a corresponding ion will also be arrested, because electric fields within the plasma will produce forces to counter any charge separation.

Havnes and Sigernes [2005] suggested that the loss of trail electrons through attachment to aerosols could decrease the observed decay times of meteor radar echoes. Furthermore, their modeling indicated that meteor trails with small initial electron line density would be more susceptible to decay time reduction. Singer *et al.* [2008] tested some of the predictions of Havnes and Sigernes [2005] and found that weaker meteor trails usually produced shorter decay times relative to strong trails around the same height

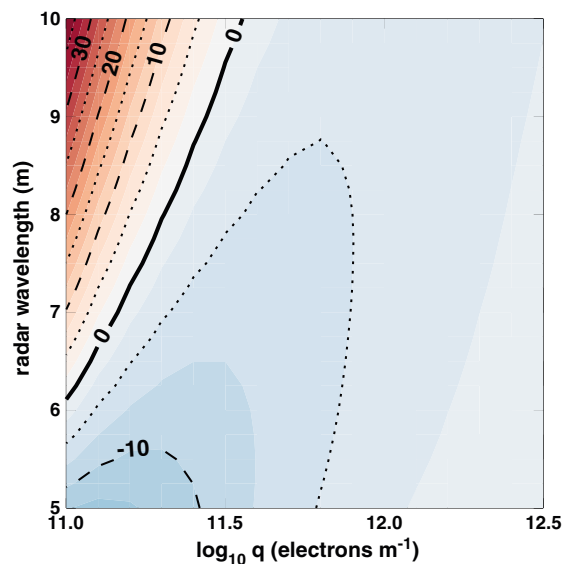


Figure 6. Percentage change to echo decay time predicted by numerical model including aerosol absorption for $D = 2\text{m}^2\text{s}^{-1}$, $n_d = 10^{10}\text{m}^{-3}$, and $R_{ed} = 10^8\text{m}^3\text{s}^{-1}$ as a function of radar wavelength and trail density, q . Dashed contours indicate 10% increments and dotted contours indicate 5% increments. Negative change (blue) indicates reduced echo decay time. Positive change (red) indicates extended echo decay time.

[McKinley, 1961], but large offsets are seen in observed diffusion coefficient profiles for strong echoes as well.

Another problem with the aerosol absorption theory is that the effect of aerosol absorption for constant aerosol density and capture rate decreases with altitude. At lower altitudes, the initial radius is smaller [Jones, 1995], which produces higher values of n_e near the trail axis. Thus, the rapid depletion of scattering electrons near the core is proportionally smaller at lower altitudes. Also, the diffusion coefficient increases exponentially with altitude, resulting in longer decay times at lower heights. The result is that aerosol absorption produces smaller proportional changes to echo decay times as altitude decreases. Lastly, it should be noted that aerosols, in general, and summertime polar mesospheric clouds (PMC), in particular, usually occur in well-defined layers [Megner *et al.*, 2006]. The observational discrepancies exhibit a smooth deviation that increases with decreasing altitude. Thus, while aerosol absorption may have some effect on meteor radar echo decay times, the predicted behavior is inconsistent with observations, indicating that aerosol absorption is not the primary mechanism responsible for the observed discrepancies.

5. Chemical Processes

The composition of meteoric plasma is not constant throughout the process of trail diffusion. Free electrons can be lost due to recombination and attachment [Kaiser, 1953], charge can be exchanged between positive ions and neutral constituents, electrons can be detached from the newly formed negative ions, and ions with opposite charge can neutralize one another. The relative effect of the different processes depends on the density of the reacting species and the rate at which the reaction occurs. Baggeley and Cummock [1974] and Plane and Whalley [2012] list a number of reactions relevant to the evolution of meteoric plasma, which have been used as the basis of the current study. These are listed with additional relevant reactions from other sources in Tables 1 and 2.

In the interest of simplicity, Mg has been used as a representative atom for meteoric metals, based on the similar value of ionic mobility to the mean value of meteoric ions [Cervera and Reid, 2000]. Additionally, the relatively long persistence of Mg^+ ions in the mesosphere [Whalley *et al.*, 2011] reduces the possibility that the model will overestimate the effects of chemical processes on underdense echo decay times. Thus, the model predictions should serve as a floor for the reduction of echo decay times due to recombination.

absorption can significantly alter the decay time of radar echoes. Depending on the wavelength, echo durations may be shortened or lengthened, depending on where electrons are being lost in the context of the Bessel weighting function. For the conditions shown in Figure 6, electron absorption by aerosols resulted in a small decrease in decay time for meteors with densities larger than about $10^{11.5}$ electrons m^{-1} . At longer wavelengths and lower trail densities, aerosol absorption was predicted to result in longer decay times through the removal of electrons in areas of the trail responsible for destructive interference.

It should be noted that even with an aggressive choice of electron capture rate and aerosol density, the effect for meteor trails with line densities greater than 10^{12}m^{-1} is negligible. This raises doubts about the viability of aerosol absorption as the dominant mechanism responsible for the observed discrepancies. Underdense echoes can be produced by meteor trails with electron line densities in excess of 10^{14}m^{-1} .

Table 1. Negative Ion Reactions Included in Numerical Simulations^a

Number	Reaction	Rate	Reference
<i>Electron Attachment</i>			
R1	$O_2 + O_2 + e \rightarrow O_2^- + O_2$	2.2×10^{-42}	<i>Shimamori and Hatano [1977]</i>
R2	$O_2 + N_2 + e \rightarrow O_2^- + N_2$	1.0×10^{-42}	<i>Chanin et al. [1959]^b</i>
R3	$O_3 + e \rightarrow O^- + O_2$	7.0×10^{-18}	<i>Fehsenfeld and Ferguson [1968]^b</i>
<i>Electron Detachment</i>			
R4	$O^- + O \rightarrow O_2 + e$	1.9×10^{-16}	<i>Ferguson et al. [1969]^b</i>
R5	$O^- + O_2^* \rightarrow O_3 + e$	3.0×10^{-16}	<i>Fehsenfeld et al. [1969a]^b</i>
R6	$O_2^- + O \rightarrow O_3 + e$	3×10^{-16}	<i>Fehsenfeld et al. [1967]^b</i>
R7	$O_2^- + O_2^* \rightarrow 2O_2 + e$	2×10^{-16}	<i>Fehsenfeld et al. [1969a]^b</i>
R8	$O_3^- + O \rightarrow 2O_2 + e$	1.0×10^{-16}	<i>Adams and Megill [1967]^b</i>
R9	$O_3^- + O_3 \rightarrow 3O_2 + e$	1.0×10^{-16}	<i>Adams and Megill [1967]^b</i>
R10	$O^- + h\nu \rightarrow O + e$	1.40	<i>Branscomb [1964]^b</i>
R11	$O_2^- + h\nu \rightarrow O_2 + e$	0.30	<i>Woo et al. [1969]^b</i>
R12	$O_3^- + h\nu \rightarrow O_3 + e$	0.06	<i>Baggaley and Cummack [1974]</i>
R13	$CO_3^- + h\nu \rightarrow CO_3 + e$	0.04	<i>Kamiyama [1970]^b</i>
R14	$NO_2^- + h\nu \rightarrow NO_2 + e$	0.04	<i>Baggaley and Cummack [1974]</i>
R15	$NO_3^- + h\nu \rightarrow NO_3 + e$	0.03	<i>Kamiyama [1970]^b</i>
<i>Negative Ion Reactions</i>			
R16	$O^- + O_3 \rightarrow O_3^- + O$	7.0×10^{-16}	<i>Fehsenfeld et al. [1967]^b</i>
R17	$O^- + 2O_2 \rightarrow O_3^- + O_2$	2.0×10^{-42}	<i>Chanin et al. [1959]^b</i>
R18	$O_2^- + O \rightarrow O^- + O_2$	1.0×10^{-17}	<i>Baggaley and Cummack [1974]</i>
R19	$O_2^- + O_3 \rightarrow O_3^- + O_2$	3.0×10^{-16}	<i>Fehsenfeld et al. [1967]^b</i>
R20	$O_2^- + O_2 + M \rightarrow O_4^- + M$	3.5×10^{-43}	<i>Pack and Phelps [1971]^b</i>
R21	$O_3^- + O \rightarrow O_2^- + O_2$	1.4×10^{-16}	<i>LeVier and Branscomb [1968]^b</i>
R22	$O_3^- + CO_2 \rightarrow CO_3^- + O_2$	4.0×10^{-16}	<i>Fehsenfeld et al. [1967]^b</i>
R23	$O_3^- + NO \rightarrow NO_2^- + O_2$	1.0×10^{-17}	<i>Baggaley and Cummack [1974]</i>
R24	$O_4^- + O \rightarrow O_3^- + O_2$	4.0×10^{-16}	<i>Fehsenfeld et al. [1969b]^b</i>
R25	$O_4^- + O_2 \rightarrow O_2^- + 2O_2$	2.0×10^{-20}	<i>Payzant and Kebarle [1972]^b</i>
R26	$O_4^- + CO_2 \rightarrow CO_4^- + O_2$	4.3×10^{-16}	<i>Fehsenfeld et al. [1969b]^b</i>
R27	$O_4^- + NO \rightarrow NO_3^- + O_2$	2.5×10^{-16}	<i>Fehsenfeld et al. [1969b]^b</i>
R28	$CO_3^- + O \rightarrow O_2^- + CO_2$	8.0×10^{-17}	<i>Fehsenfeld et al. [1967]^b</i>
R29	$CO_3^- + N \rightarrow NO_2^- + CO_2$	9.0×10^{-18}	<i>Fehsenfeld et al. [1967]^b</i>
R30	$CO_4^- + O \rightarrow CO_3^- + O_2$	1.5×10^{-16}	<i>Fehsenfeld et al. [1969b]^b</i>
R31	$CO_4^- + O_3 \rightarrow O_3^- + CO_4$	1.0×10^{-16}	<i>Arnold and Krankowsky [1971]^b</i>
R32	$CO_4^- + NO \rightarrow NO_3^- + CO_2$	4.8×10^{-17}	<i>Fehsenfeld et al. [1969b]^b</i>
R33	$NO_2^- + O_3 \rightarrow NO_3^- + O_2$	1.8×10^{-17}	<i>Fehsenfeld and Ferguson [1968]^b</i>
R34	$NO_2^- + NO_2 \rightarrow NO_3^- + NO$	4.0×10^{-18}	<i>Baggaley and Cummack [1974]</i>
R35	$NO_3^- + NO \rightarrow NO_2^- + NO_2$	1.5×10^{-17}	<i>Baggaley and Cummack [1974]</i>

^aTwo-body reaction coefficients are in units of $m^3 s^{-1}$. Three-body reactions coefficients are in units of $m^6 s^{-1}$. Photo-ionization coefficients are in units of s^{-1} . M = O_2 , N_2 .

^bReference via *Baggaley and Cummack [1974]*.

Baggaley [1979] examined the scenario of recombinative loss and concluded that recombination has no effect on the decay time of underdense meteors. That study, however, was restricted to meteors above 90 km, which combine short decay times with low background density. It is unsurprising then, that such a population of meteors would be unaffected by chemical processes. Other work did, however, indicate that recombination and attachment processes will constrain the decay times of overdense meteors [*Baggaley, 1978*], with increasing severity at lower altitudes. This can also be seen in *Davis [1959]* and *Baggaley [1979a]*, which show that overdense echo decay times at low altitudes are severely constrained by deionization.

The most direct path for the loss of free electrons is by photorecombination, whereby free electrons recombine with the original atomic ions in the meteoric plasma. The recombination of electrons with positive trail atomic ions is very slow, however, due to the small photorecombination cross section for atomic ions and electrons. In contrast, dissociative recombination, in which a positive molecular ion is separated into its component atoms during the recombination process has a much higher reaction rate. The positive molecular ions consumed during dissociative recombination are created primarily through charge transfer,

Table 2. Positive Ion and Neutralization Reactions Included in Numerical Simulations^a

Number	Reaction	Rate	Reference
<i>Positive Ion Reactions</i>			
R36	$\text{Mg}^+ + \text{O}_3 \rightarrow \text{MgO}^+ + \text{O}_2$	1.2×10^{-16}	Whalley et al. [2011]
R37	$\text{Mg}^+ + \text{O}_2 + \text{M} \rightarrow \text{MgO}_2^+ + \text{M}$	$4.1 \times 10^{-43} (T/300)^{-1.65}$	Whalley et al. [2011]
R38	$\text{Mg}^+ + 2\text{N}_2 \rightarrow \text{MgN}_2^+ + \text{N}_2$	$2.7 \times 10^{-43} (T/300)^{-1.88}$	Whalley et al. [2011]
R39	$\text{Mg}^+ + \text{CO}_2 + \text{M} \rightarrow \text{MgCO}_2^+ + \text{M}$	$7.3 \times 10^{-42} (T/300)^{-1.59}$	Whalley et al. [2011]
R40	$\text{MgO}^+ + \text{O} \rightarrow \text{Mg}^+ + \text{O}_2$	5.9×10^{-16}	Ferguson and Fehsenfeld [1968] ^b
R41 ^c	$\text{MgO}^+ + \text{O}_3 \rightarrow \text{Mg}^+ + 2\text{O}_2$	8.5×10^{-16}	Whalley et al. [2011]
R42 ^c	$\text{MgO}^+ + \text{O}_3 \rightarrow \text{MgO}_2^+ + \text{O}_2$	8.5×10^{-16}	Whalley et al. [2011]
R43	$\text{MgO}^+ + \text{N}_2 + \text{M} \rightarrow \text{MgON}_2^+ + \text{M}$	$5.1 \times 10^{-42} (T/300)^{-2.76}$	Whalley et al. [2011]
R44	$\text{MgO}_2^+ + \text{O} \rightarrow \text{MgO}^+ + \text{O}_2$	1.0×10^{-16}	Baggaley and Cummack [1974]
R45	$\text{MgN}_2^+ + \text{O}_2 \rightarrow \text{MgO}_2^+ + \text{N}_2$	3.5×10^{-18}	Whalley et al. [2011]
R46	$\text{MgCO}_2^+ + \text{O}_2 \rightarrow \text{MgO}_2^+ + \text{CO}_2$	2.2×10^{-18}	Whalley and Plane [2010]
R47	$\text{Mg} + \text{O}_2^+ \rightarrow \text{Mg}^+ + \text{O}_2$	1.2×10^{-15}	Rutherford et al. [1971]
R48	$\text{Mg} + \text{NO}^+ \rightarrow \text{Mg}^+ + \text{NO}$	8.2×10^{-16}	Rutherford et al. [1971]
R49	$\text{O}^+ + \text{O}_2 \rightarrow \text{O}_2^+ + \text{O}$	2.5×10^{-17}	Lindinger et al. [1974]
R50	$\text{O}^+ + \text{N}_2 \rightarrow \text{NO}^+ + \text{N}$	2.0×10^{-18}	Lindinger et al. [1974]
<i>Electron-Ion Recombination</i>			
R51	$\text{Mg}^+ + e \rightarrow \text{Mg} + h\nu$	3.0×10^{-18}	Bates [1962] ^b
R52	$\text{Mg}^+ + \text{M} + e \rightarrow \text{Mg} + \text{M}$	1.0×10^{-38}	Danilov et al. [1959] ^b
R53	$\text{MgO}^+ + e \rightarrow \text{Mg} + \text{O}$	$3.0 \times 10^{-13} (T/200)^{-0.5}$	Plane and Whalley [2012]
R54	$\text{MgO}_2^+ + e \rightarrow \text{Mg} + \text{O}_2$	3.0×10^{-13}	Swider [1969] ^b
R55	$\text{MgN}_2^+ + e \rightarrow \text{Mg} + \text{N}_2$	$3.0 \times 10^{-13} (T/200)^{-0.5}$	Plane and Whalley [2012]
R56	$\text{MgCO}_2^+ + e \rightarrow \text{Mg} + \text{CO}_2$	$3.0 \times 10^{-13} (T/200)^{-0.5}$	Plane and Whalley [2012]
R57	$\text{O}_2^+ + e \rightarrow \text{O} + \text{O}$	2.2×10^{-13}	Walls and Dunn [1974]
R58	$\text{NO}^+ + e \rightarrow \text{N} + \text{O}$	7.0×10^{-13}	Walls and Dunn [1974]
<i>Ion-Ion Neutralization</i>			
R59	$\text{X}^+ + \text{O}^- \rightarrow \text{X} + \text{O}$	1.0×10^{-18}	Baggaley and Cummack [1974]
R60	$\text{X}^+ + \text{AB}^- \rightarrow \text{X} + \text{AB}$	1.0×10^{-13}	Baggaley and Cummack [1974]
R61	$\text{XO}^+ + \text{O}^- \rightarrow \text{XO} + \text{O}$	1.0×10^{-13}	Baggaley and Cummack [1974]
R62	$\text{XO}^+ + \text{AB}^- \rightarrow \text{XO} + \text{AB}$	1.0×10^{-13}	Baggaley and Cummack [1974]
R63	$\text{XO}_2^+ + \text{O}^- \rightarrow \text{XO}_2 + \text{O}$	1.0×10^{-13}	Baggaley and Cummack [1974]
R64	$\text{XO}_2^+ + \text{AB}^- \rightarrow \text{XO}_2 + \text{AB}$	1.0×10^{-13}	Baggaley and Cummack [1974]

^aTwo-body reaction coefficients are in units of m^3s^{-1} . Three-body reactions coefficients are in units of m^6s^{-1} . Photo-ionization coefficients are in units of s^{-1} . $\text{M} = \text{O}_2, \text{N}_2$.

^bReference via Baggaley and Cummack [1974].

^cBranching ratios for $\text{MgO}^+ + \text{O}_3$ to produce Mg^+ and MgO_2^+ are 0.35 and 0.65, respectively.

whereby the primary atomic ions initially present in the trail transfer positive charge to neutral atmospheric constituents. The resultant positive molecular ions are then rapidly destroyed through dissociative recombination, as listed in reactions R52–R58.

While O_2^+ and NO^+ are present in the daytime *D* region ionosphere in small quantities, meteor trails also produce O_2^+ and NO^+ through charge transfer reactions of O^+ with atmospheric O_2 and N_2 , respectively. Also of importance to the fate of free electrons in meteor trails are the molecular ions formed by the attachment of metal atomic ions to atmospheric constituents. Ozone rapidly converts Mg^+ to MgO^+ , while three-body reactions with O_2 and N_2 produce MgO_2^+ .

Negative ion formation occurs through the attachment of free electrons to neutral atmospheric constituents. This can occur through the reaction $\text{O}_3 + e \rightarrow \text{O}^- + \text{O}_2$, but more significant are the three-body reaction rates R1 and R2 of Table 1 where electrons are lost to attachment to O_2 and N_2 . Although these two reactions have small reaction rates, the removal of electrons to three-body attachment scales with the square of neutral density. Hence, negative ion formation is rapid at low altitudes, where it plays a prominent role in meteoric ion chemistry. The subsequent reactions between negative ions and neutral constituents, listed as R16–R35 in Table 1 produce more reactive ions that return negative charge to be available for chemical processes, as well as producing long-lived negative ions such as NO_3^- and CO_4^- that effectively lock away free electrons for the duration of trail diffusion [Baggaley and Cummack, 1974].

5.1. Chemical Numerical Model

The evolution of underdense meteor trails in the context of the processes listed in Tables 1 and 2 was evaluated using a numerical model. Meteor trails were assumed to initially have a Gaussian radial density distribution. The densities of the 26 different constituents were modeled assuming identical diffusion coefficients and the 64 different reactions. The simulation was run using Mg^+ as the only meteoric ion and also for trails composed of an equal mixture of Mg^+ and O^+ .

The use of a single diffusion coefficient avoided a prohibitive computational burden that would come with including differential diffusion in the solution. Furthermore, Jones and Jones [1990] showed that differential diffusion of ionic species does not significantly distort the shape of the electron density distribution. Younger et al. [2013] determined that the presence of free electrons retards the development of differential diffusion and that the decay times of meteor trails with multiple ionic species show little deviation from the case of a single species with an average diffusion coefficient.

An ozone concentration profile was constructed based on the results of Smith et al. [2013], consisting of a 5 km wide layer, centered at 90 km, with a peak concentration of 10 ppm. Similarly, the atomic oxygen profile was based on the profiles shown in Mlynarczyk et al. [2013], represented in the model as a 5 km wide layer centered at 95 km, with a peak density of $6 \times 10^{17} \text{ m}^{-3}$. Mg^+ was used as a representative ion for meteoric material, based on its central value of ionic mobility [Mason and McDaniel, 1988] and common presence in meteoric ions [Jones, 1997]. Peak densities of O and O_3 at the upper limit of plausibility were chosen so as to establish an upper bound for the effects of the two species. CO_2 was set to a fixed concentration of 0.35 ppm and the density of NO was held constant at $6 \times 10^{13} \text{ m}^{-3}$ at all heights [Baggaley and Cummock, 1974].

The diffusion and chemical evolution of the meteor trail and background atmosphere were calculated by simultaneously solving the equations

$$\frac{\partial n_i}{\partial t} = \frac{D}{r} \frac{\partial}{\partial r} \left(r \frac{\partial n_i}{\partial r} \right) - \sum_{j \neq i} \alpha_{ji} n_i n_j - \sum_{j \neq i} \beta_{ji} n_i n_j + \sum_{j \neq i} \gamma_{ij} n_i n_j \quad (6)$$

for the 26 species using a fourth-order Runge-Kutta method, where α is the recombination rate, β is the attachment rate, and γ is the detachment rate. A fixed time step of 0.1 ms was used with a spatial basis comprised of 160 points with a spacing of $r_0/20$. The calculation was performed for a diffusion coefficient range of $\log_{10} D = -0.8 - 0.2$, assuming an isothermal atmosphere at 180 K. The simulation was run at each density for wavelengths between 5 and 9 m until the predicted radar backscatter power was reduced by a factor of $\exp(-1)$ from the initial maximum value.

The diffusion component of the model was checked by running the model with all reaction rates set to zero and comparing the predicted decay times with the theoretical values from equation (3). The chemical reaction component of the model was verified by checking that quasi-neutrality was maintained at all times, i.e., that the net positive charge was equal to the net negative charge and that all species were conserved throughout the reactions. The size of the spatial and temporal steps were checked by monitoring the stability of the solutions and through comparison to different step sizes. The relative impact of different reactions was assessed by selectively disabling different reactions and species.

5.2. Chemical Simulation Results

A set of representative results of the numerical model can be seen in Figure 7. When chemical processes were combined with diffusion, the predicted effects can be separated into two distinct regimes. At higher altitudes, chemical processes in the model produced a deviation in diffusion coefficient estimates that increased with decreasing altitude at an approximately fixed rate, i.e., producing an erroneously high value of the estimated diffusion coefficient gradient $\partial \log D / \partial z$. When O^+ was included as a trail ion (Figures 7a, 7b, and 7d), there was a significant fixed offset between the decay time estimate of $\log D$ and the true value.

Meteor trails with lower electron line density were less affected in the model, displaying less offset from the true diffusion coefficient profile, a lower height at which the gradient of the diffusion coefficient estimate profile reversed, and a better agreement with the true diffusion coefficient gradient above the turnaround height. The deviation of the diffusion coefficient gradient estimates increased with larger radar wavelengths. At lower altitudes, the inclusion of chemical effects in the model produced a reversal in the gradient of $\log D$

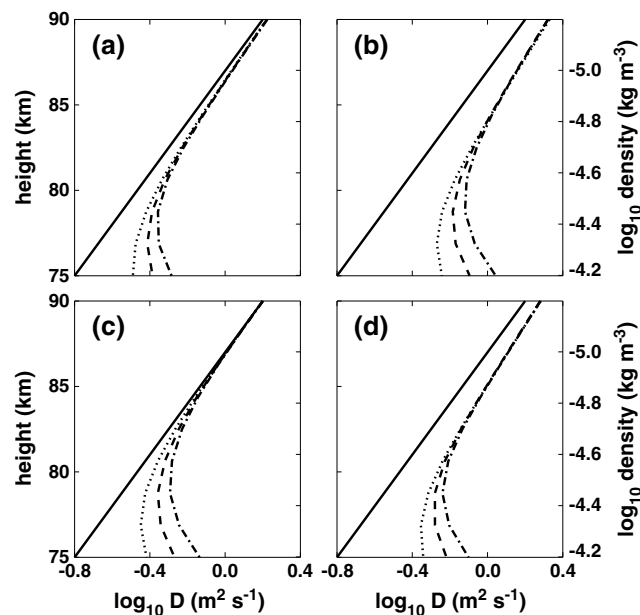


Figure 7. Model predictions of diffusion coefficient estimates based on simulated echo decay times for (a) $q = 10^{13} \text{ m}^{-1}$, (b) $q = 10^{14} \text{ m}^{-1}$, (c) $q = 5 \times 10^{13} \text{ m}^{-1}$ without trail O^+ , and (d) $q = 5 \times 10^{13} \text{ m}^{-1}$ without atmospheric O_3 , as observed with 5 m (dotted), 7 m (dashed), and 9 m (dash-dotted) wavelength radars. Solid line indicates the true atmospheric diffusion coefficient of the model.

expected from the $1/\rho$ proportionality of the diffusion coefficient. The critical density at which the gradients $\partial \log \tau / \partial z$ and $\partial \log D / \partial z$ change signs is a function of initial meteor trail electron line density and radar wavelength. Meteors with smaller initial electron line densities and radars with smaller wavelengths display higher critical densities, which corresponds to lower gradient reversal altitudes.

Neutral atomic oxygen plays a role in moderating the effects of both positive and negative molecular ion formation. Through reactions R40 and R44, positive molecular ions that would otherwise recombine with electrons are destroyed and Mg^+ is returned to the trail. For less prominent constituents, reactions R21 and R24 inhibit the formation of large quantities of O_3^- and reactions R28 and R30 rapidly eliminate CO_3^- , although the supply of neutral atomic oxygen will be exhausted over the course of longer decay times. Overall, the effect of background atomic oxygen at the densities considered is not sufficient to significantly alter the diffusion coefficient estimate profile.

Table 3 displays the final ion densities of the chemical model for a point above the critical density and a point below the critical density. Both trails experience substantial deionization during the decay process, with the lower altitude trail experiencing more recombination. In both cases, O^+ is completely consumed in the early stages of trail development. Both cases also show that the primary Mg^+ path is via the formation of MgO_2^+ , which is consistent with the laboratory results of Whalley *et al.* [2011].

The difference in total ion densities between the two simulated trails is due primarily to the reduction in free electron density for negative ions and the reduction of Mg^+ and O_2^+ for positive ions. Free electrons are lost through recombinaive processes. For the case of positive ions, Mg^+ is consumed through the formation and subsequent dissociative recombination of MgO_2^+ , while additional O_2^+ is removed through dissociative recombination during the longer decay time incurred by a smaller diffusion coefficient.

6. Dominant Neutralization Paths

At higher altitudes, the presence of ozone leads to the rapid deionization of meteoric plasma [Baggaley and Cumack, 1974] through the reaction



estimates. The predictions of the model generally agree with observations, as can be seen from a comparison of Figure 7 with Figures 1 and 3, but the wavelength dependence of the fixed offset seen between estimates of $\log D$ for different wavelengths seen in Figure 2 was not reproduced.

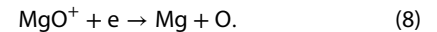
The relative impacts of different reactions on echo decay time/diffusion coefficient estimate profiles were assessed by running the numerical simulation with different reactions disabled. The effect of O^+ is to cause an approximately fixed reduction in $\log \tau$ and, hence, $\log D$ at all heights. This predicted offset does not vary significantly between different radar wavelengths.

The effect of three-body attachment is apparent at lower altitudes, where it causes a reversal in the gradient of $\log D$. Below a critical height, the model predicts that echo decay times will decrease with decreasing altitude, which is the opposite of what would be

Table 3. Calculated Abundance of Different Ion Species Following 9 m Wavelength Echo Decay for Two Different Heights With an Initial Trail Density of $5 \times 10^{13} \text{ el m}^{-1}$

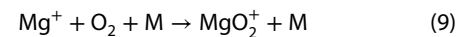
$\log_{10} D = 0 \text{ m}^2 \text{ s}^{-1}, \tau = 0.68 \text{ s}$			
Negative Ions (m^{-1})		Positive Ions (m^{-1})	
e^-	2.9×10^{13}	Mg^+	1.7×10^{13}
O^-	1.3×10^{10}	O^+	0
O_2^-	4.3×10^{12}	O_2^+	9.6×10^{12}
O_3^-	4.0×10^6	MgO^+	1.4×10^{11}
O_4^-	1.6×10^9	MgO_2^+	6.0×10^{12}
CO_3^-	2.7×10^9	MgN_2^+	9.8×10^9
CO_4^-	8.5×10^{10}	MgCO_2^+	2.0×10^7
		NO^+	8.6×10^{11}
total	3.3×10^{13}	total	3.3×10^{13}
$\log_{10} D = -0.6 \text{ m}^2 \text{ s}^{-1}, \tau = 1.52 \text{ s}$			
Negative Ions (m^{-1})		Positive Ions (m^{-1})	
e^-	1.7×10^{13}	Mg^+	9.6×10^{12}
O^-	3.4×10^{10}	O^+	0
O_2^-	4.6×10^{12}	O_2^+	4.4×10^{12}
O_3^-	5.1×10^6	MgO^+	3.1×10^{11}
O_4^-	1.7×10^9	MgO_2^+	7.4×10^{12}
CO_3^-	1.6×10^{10}	MgN_2^+	5.7×10^9
CO_4^-	2.2×10^{11}	MgCO_2^+	1.2×10^7
		NO^+	2.2×10^{11}
total	2.2×10^{13}	total	2.2×10^{13}

which leads to the removal of electrons through the dissociative recombination reaction

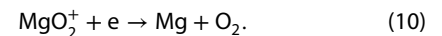


This reaction path is responsible for the relative lack of long-duration overdense meteor detections that would otherwise be expected [Kaiser, 1953]. The constraint of long-duration overdense meteor echoes by ozone-initiated neutralization can be used to estimate ozone concentration in the mesosphere as shown, for example, by Jones *et al.* [1990] and Cevolani and Pupillo [2003]. It should be noted, at this point, that the long echo durations of overdense meteors are produced by a different scattering mechanism than the exponential echo decay associated with short-lived underdense meteors. The model calculations predicted that ozone is of relatively minor importance for underdense meteors, due to the small combined concentration of ozone and meteoric plasma.

At lower altitudes the density-squared dependence of the three-body attachment reaction



will eventually overtake positive ion loss to ozone, leading to electron-ion neutralization through the reaction



The electron-ion recombination rates are similar for dissociative recombination with MgO^+ and MgO_2^+ and are much faster than the production rates of the two positive molecular ions, which establishes molecular ion production as the primary limiting factor in the rate of ion-electron recombination. Therefore, a criterion for ozone concentration and neutral density can be established, at which ozone-ion attachment transitions to three-body positive ion attachment as the dominant source of electron-ion recombination sites.

Three-body attachment takes over as the dominant path for electron loss when

$$\frac{\text{O}_3}{\text{N}_2^2} = \frac{R36}{p_{\text{O}_2} R37 + R38}, \quad (11)$$

where $p_{\text{O}_2} \approx 0.25$ is the fractional concentration of O_2 relative to N_2 . This leads to a critical N_2 density at which attachment loss transitions from being ozone dominated to neutral dominated. For an ozone concentration of 1 ppm, the N_2 density at which this transition occurs is approximately $1.3 \times 10^{20} \text{ m}^{-3}$. At an ozone concentration of 10 ppm, the transition density is about $1.3 \times 10^{21} \text{ m}^{-3}$.

This assumes, however, that the attachment process is permanent. Examining the fate of MgO^+ , MgN_2^+ , and MgO_2^+ ions after formation it can be seen that MgO^+ is converted back to Mg^+ and O_2 by reaction with atomic oxygen in reaction R40. In contrast, MgN_2^+ is converted to MgO_2^+ in reaction R45 and MgO_2^+ is converted to MgO^+ via reaction with O in reaction R44, providing additional opportunities for dissociative recombination in the reaction chain. This also highlights the difficulty of producing a single term to correct echo decay times, as suggested by Kaiser [1953]. Given the coupled and cyclical nature of the dominant reactions in low-altitude underdense meteor trains, a simple linear model of attachment losses is no longer valid.

The molecular ions formed by the attachment of metallic ions to ozone can be returned to the original monatomic ion state through a single reaction. Ions formed through attachment to neutral molecules require more steps to return to the original Mg^+ ion. Thus, the products of neutral attachment paths for positive ions will be susceptible to dissociative recombination for longer periods than the MgO^+ ions formed

via attachment to ozone. This indicates that the true neutral transition density for ozone dominance is lower than the estimate shown above and is also dependent on the atomic oxygen density.

7. Discussion

Estimates of the ambipolar diffusion coefficient produced from underdense meteor radar echo decay times are significantly impacted by nondiffusion processes in the lower portion of the meteor ablation region. Chemical reactions occur at all heights that result in a reduction in echo decay times. The presence of O^+ in meteor trails results in a fixed reduction to $\log \tau$, resulting from the rapid dissociative recombination with the resultant O_2^+ and NO^+ . Diffusion coefficient gradients are affected by these processes to a small degree, but it is likely that the temperature gradient climatologies necessary to use diffusion coefficient gradients for temperature measurements [Hocking *et al.*, 2004] compensate for this.

Numerical simulations of diffusion with chemical processes indicate that three-body attachment between positive metallic ions and neutral atmospheric molecules distorts diffusion coefficient estimates at low altitudes. The reduction in decay time due to three-body attachment is large enough to change the sign of $\partial \log \tau / \partial z$ and $\partial \log D / \partial z$ below a critical neutral density. The strong influence of an attachment process with a density-squared height dependence, which is also temporally invariant to solar illumination conditions [McIntosh and Hajduk, 1977], is seen in observations to be an excellent marker of constant density surface height. As such, the inflection point in $\log \tau$ or $\log D$ profiles may be a useful parameter for tracking atmospheric density variations.

The reduction in $\log \tau$ predicted in the chemical model at all altitudes due to the presence of O^+ in the trail draws attention to the importance on nonmetallic positive ions in meteor trails. Given the high oxygen content of meteors, coupled with the presence of atmospheric oxygen, it is likely that the impact of O^+ and O_2^+ is a significant sink for free electrons in meteor trails that should be included in any consideration of meteoric plasma chemistry [Baggaley, 1979].

The previous work on aerosol absorption has been revisited in the context of independent measurements from the MLS instrument aboard the Aura EOS satellite. As shown in Figure 1, denser trails show worse agreement with MLS data, compared to weaker trails. While this would seem to contradict the observations of Younger *et al.* [2008], the data are actually consistent. The previous study used the agreement between the diffusion coefficient estimates from radars with different frequencies as an indication of the quality of the estimates. What has been shown using the comparison to MLS data is that strong meteors provide better agreement between different radar frequencies of a biased estimate. Weaker meteor trails provide worse agreement between the two radars, but the estimates of the diffusion coefficient are closer to the MLS values.

This is not to say, however, that aerosols play no role in meteor trail evolution, but rather that aerosol absorption is not the dominant mechanism responsible for the significant discrepancies seen in observations at all times. Figure 4 displays increased deviations between radar and MLS estimates of D during summer, which may be due to the presence of ice crystals related to PMC/noctilucent clouds and polar mesospheric summer echoes (PMSE). At the low temperatures present around the polar mesopause in summer, the aggregation of ice crystals may result in a significant increase in the electron capture rate of atmospheric aerosols. Regardless of enhancements though, aerosol absorption remains insufficient to explain the substantial reduction in underdense meteor radar echo decay times seen at low altitudes at all times of the year.

The key difference between the attachment of free electrons to aerosols and the attachment of positive ions to neutral molecules is the relative abundance of absorbers. In the case of aerosols, the density of available aerosol particles can be of a similar order of magnitude to the density of meteor trail electrons. For neutral molecules, the density is significantly higher than the trail plasma density, ensuring that the supply of neutral molecules available for attachment is never depleted. This is compounded by the rate of three-body attachment, which is proportional to the square of atmospheric density, whereas the rate of aerosol absorption only scales linearly with aerosol density.

Observations and numerical modeling indicate that, while affected by deionization effects, the diffusion coefficient gradient method of temperature estimation is still valid above 85 km. Direct estimates of temperature extracted from the climatology method remain more problematic, though, given the substantial

effects of chemical reactions seen at all altitudes. Numerical modeling and comparisons between meteor radar and MLS satellite observations show significant disparities between meteor radar estimates and the true value of D , although the deviation of meteor radar diffusion coefficient estimates is reduced at higher radar frequencies.

Previous studies of the interaction between meteoric plasma and atmospheric ozone have focused on dense meteors at higher altitudes. The results of numerical simulations indicate that the deionization of low-altitude underdense meteors is dominated by attachment to neutral molecules due to the higher density of neutral molecules and the longer exposure to dissociative recombination of the sequence of molecular ions produced by three-body recombination. The complex interaction of multiple coupled and cyclical reaction chains prevents the use of a single-attachment correction term, as suggested by Kaiser [1953], to adjust low-altitude underdense meteor diffusion coefficients, although it does remain valid for dense meteors at high altitudes with long echo durations constrained by ozone effects.

8. Conclusions

Our findings are summarized as follows:

1. Diffusion coefficient estimates based on meteor radar echo decay times are frequency dependent and are large compared to estimates derived from satellite measurements.
2. The height at which the gradient of meteor radar echo decay times reverses is closely correlated with a constant density surface.
3. Aerosol absorption may play a role in the reduction of meteor decay times under certain conditions, but aerosol effects are not sufficient to explain the severe reduction to low-altitude meteor radar echo decay times seen at all times.
4. Observations are consistent with numerical simulations of meteor trail diffusion including chemical processes, which indicates that the reduction to echo decay times of low-altitude meteors is due to neutralization of meteoric ionization. This process is initiated primarily through three-body attachment of positive meteoric ions to neutral atmospheric molecules.
5. The role of ozone, while significant for dense meteors at higher altitudes, is of relatively minor importance for underdense meteors in the lower part of the meteor region.

While meteor plasma deionization frustrates attempts to use underdense meteor radar echo decay times for a simple diagnostic atmospheric parameter, it has been shown that they also provide an opportunity to examine more complex phenomena. The presence of severe underdense meteor radar echo decay time reduction at low altitudes contains information on attachment rates and can be used to infer the height of constant density surfaces. Thus, the observational discrepancies with the diffusion-only model of underdense meteor trail evolution provide new opportunities for mesospheric research, such as the exploitation of the height of gradient reversal to track variations in atmospheric density. Future work should focus on the problems of correcting meteor radar diffusion coefficient estimates for the deionization effects and determining the precise impact of deionization on the gradient temperature method, both of which will necessarily involve inferring an effective ion loss rate. Additional observations by colocated meteor radars with different frequencies will be a vital component of this endeavor.

References

- Adams, G. W., and L. R. Megill (1967), A two-ion D-region model for polar cap absorption events, *Planet. Space Sci.*, **15**, 1111–1130.
- Amyx, K., Z. Sternovskya, S. Knappmiller, S. Robertson, M. Horanyi, and J. Gumbel (2008), In-situ measurement of smoke particles in the wintertime polar mesosphere between 80 and 85 km altitude, *J. Atmos. Sol. Terr. Phys.*, **70**, 61–70.
- Arnold, F., and D. Krankowsky (1971), Negative ions in the lower ionosphere: A comparison of a model computation and a mass-spectrometric measurement, *J. Atmos. Terr. Phys.*, **33**, 1693–1702.
- Baggaley, J. (2009), Meteoric ionization: The interpretation of radar trail echoes, *Radio Sci. Bull.*, **329**, 6–20.
- Baggaley, W. J. (1978), The de-ionization of dense meteor trains, *Planet. Space Sci.*, **26**, 979–981.
- Baggaley, W. J. (1979), The influence of recombination on under-dense radio-meteor data, *Planet. Space Sci.*, **27**, 905–907.
- Baggaley, W. J. (1979a), The interpretation of overdense radio meteor echo duration characteristics, *B. Astron. I. Czech.*, **30**, 184–189.
- Baggaley, W. J., and C. H. Cummack (1974), Meteor train ion chemistry, *J. Atmos. Terr. Phys.*, **36**, 1768–1773.
- Bates, D. R. (1962), *Atomic and Molecular Processes*, vol. 13, Academic Press, New York.
- Branscomb, L. M. (1964), A review of photodetachment and related negative ion processes relevant to aeronomy, *Ann. Geophys.*, **20**, 88–105.
- Cepelca, Z., J. Borovička, W. G. Elford, D. O. ReVelle, R. L. Hawkes, V. Porubčan, and M. Šimek (1998), Meteor phenomena and bodies, *Space Sci. Rev.*, **84**, 327–471.

Acknowledgments

This study has been supported by Australian Research Council grants DP0878144 and DP1096901 and ASAC grant 2325. Additional funding was provided by the National Research Foundation of Korea grant funded by the Korea government (MEST) and also by Korea Polar Research Institute (PE14010). The authors would like to thank the Aura MLS team for providing the geopotential height and temperature measurements used in this study. The authors would also like to thank Graham Elford for his constructive discussions and John Plane for his helpful advice. Aura MLS data are available from <http://disc.sci.gsfc.nasa.gov/Aura/data-holdings/MLS>. Meteor radar data are available from The University of Adelaide and the Australian Antarctic Division upon request.

- Cervera, M. A., and I. M. Reid (2000), Comparison of atmospheric parameters derived from meteor observations with CIRA, *Radio Sci.*, **35**(3), 833–843.
- Cevolani, G., and G. Pupillo (2003), Ground-based radio observations to probe the ozone content in the meteor region, *Ann. Geophys.*, **46**, 247–258.
- Chanin, L. M., A. V. Phelps, and M. A. Biondi (1959), Measurement of the attachment of low-energy electrons to oxygen molecules, *Phys. Rev.*, **128**, 219–230.
- Cho, J. Y. N., and J. Röttger (1997), An updated review of polar mesosphere summer echoes: Observation, theory, and their relationship to noctilucent clouds and subvisible aerosols, *J. Geophys. Res.*, **102**, 2001–2020.
- Danilov, J., J. S. Greenhow, and J. E. Hall (1959), The effect of attachment on radio echo observations of meteors, *Proc. R. Soc. London, Ser. A*, **253**, 130–139.
- Davis, A. D. (1959), *Chemistry of the Ionosphere*, Plenum Press, New York.
- Decker, B. L. (1986), *World Geodetic System 1984*, Def. Mapp. Agency Aerosp. Cent., St. Louis AFS, Mo.
- Fehsenfeld, F. C., and E. E. Ferguson (1968), Further laboratory measurements of negative reactions of atmospheric interest, *Planet. Space Sci.*, **16**, 701–702.
- Fehsenfeld, F. C., A. L. Schmeltekopf, H. I. Schiff, and E. E. Ferguson (1967), Laboratory measurements of negative ion reactions of atmospheric interest, *Planet. Space Sci.*, **15**, 373–379.
- Fehsenfeld, F. C., D. L. Albritton, J. A. Burt, and H. I. Schiff (1969a), Associative-detachment reactions of O^- and O_2^- by $O_2(^1\Delta_g)$, *Can. J. Chem.*, **2**, 1793–1795.
- Fehsenfeld, F. C., E. E. Ferguson, and D. K. Bohme (1969b), Additional flowing afterglow measurements of negative ion reactions of D-region interest, *Planet. Space Sci.*, **17**, 1759–1762, doi:10.1016/0032-0633(69)90052-X.
- Ferguson, E. E., and F. C. Fehsenfeld (1968), Some aspects of the metal ion chemistry of the Earth's atmosphere, *J. Geophys. Res.*, **73**, 6215–6223.
- Ferguson, E. E., F. C. Fehsenfeld, and A. L. Schmeltekopf (1969), Ion-molecule reaction rates measured in a discharge afterglow, *Adv. Chem. Ser.*, **80**, 83–91.
- Havnes, O., and F. Sigernes (2005), On the influence of background dust on radar scattering from meteor trails, *J. Atmos. Sol. Terr. Phys.*, **67**, 659–664.
- Herlofson, N. (1947), The theory of meteor ionization, *Rep. Prog. Phys.*, **11**, 444–454.
- Hocking, W. K. (1999), Temperatures using radar-meteor decay times, *Geophys. Res. Lett.*, **26**(21), 3297–3300.
- Hocking, W. K. (2011), A review of mesosphere-stratosphere-troposphere (MST) radar developments and studies, circa 1997–2008, *J. Atmos. Sol. Terr. Phys.*, **73**, 848–882, doi:10.1016/j.jastp.2010.12.009.
- Hocking, W. K., W. Singer, J. Bremer, N. J. Mitchell, P. Batista, B. Clemesha, and M. Donner (2004), Meteor radar temperatures at multiple sites derived with SKIYMET radars and compared to OH, rocket and lidar measurements, *J. Atmos. Sol. Terr. Phys.*, **66**, 585–593, doi:10.1016/j.jastp.2004.01.011.
- Holdsworth, D. A. (2005), Angle of arrival estimation for all-sky interferometric meteor radar systems, *Radio Sci.*, **40**, RS6010, doi:10.1029/2005RS003245.
- Holdsworth, D. A., I. M. Reid, and M. A. Cervera (2004), Buckland Park all-sky interferometric meteor radar, *Radio Sci.*, **39**, RS5009, doi:10.1029/2003RS003014.
- Holdsworth, D. A., D. J. Murphy, I. M. Reid, and R. J. Morris (2008), Antarctic meteor observations using the Davis MST and meteor radars, *Adv. Space Res.*, **42**(1), 143–154, doi:10.1016/j.asr.2007.02.037.
- Jones, J., B. A. McIntosh, and M. Simeck (1990), Ozone and the duration of overdense radio meteors, *J. Atmos. Terr. Phys.*, **52**, 253–258.
- Jones, J., A. R. Webster, and W. K. Hocking (1998), An improved interferometer design for use with meteor radars, *Radio Sci.*, **33**, 55–66.
- Jones, W. (1995), Theory of the initial radius of meteor trains, *Mon. Not. R. Astron. Soc.*, **275**, 812–818.
- Jones, W. (1997), Theoretical and observational determinations of the ionization coefficient of meteors, *Mon. Not. R. Astron. Soc.*, **288**, 995–1003.
- Jones, W., and J. Jones (1990), Ionic diffusion in meteor trains, *J. Atmos. Terr. Phys.*, **52**, 185–191.
- Kaiser, T. R. (1953), Radio echo studies of meteor ionization, *Adv. Phys.*, **2**, 495–544, doi:10.1080/00018735300101282.
- Kalashnikova, O., M. Horgny, G. E. Thomas, and O. B. Toon (2000), Meteoric smoke production in the atmosphere, *Geophys. Res. Lett.*, **27**, 3293–3296.
- Kamiyama, H. (1970), Negative ion densities in chemical equilibrium in the D-region, *J. Geomagn. Geoelec.*, **22**, 403–411.
- Kim, J.-H., Y. H. Kim, C. S. Lee, and G. Jee (2010), Seasonal variation of meteor decay times observed at King Sejong Station (62.22°S, 58.78°W), Antarctica, *J. Atmos. Sol. Terr. Phys.*, **72**, 883–889.
- Klekociuk, A., R. J. Morris, and J. L. Innis (2008), First Southern Hemisphere common-volume measurements of PMC and PMSE, *Geophys. Res. Lett.*, **35**, L24804, doi:10.1029/2008GL035988.
- Lee, C. S., J. P. Younger, I. M. Reid, Y. H. Kim, and J.-H. Kim (2013), The effect of recombination and attachment on meteor radar diffusion coefficient profiles, *J. Geophys. Res. Atmos.*, **118**, 3037–3043, doi:10.1002/jgrd.50315.
- LeVier, R. E., and L. M. Branscomb (1968), Ion chemistry governing mesospheric electron concentrations, *J. Geophys. Res.*, **73**, 27–41.
- Lindinger, W., F. C. Fehsenfeld, A. L. Schmeltekopf, and E. E. Ferguson (1974), Temperature dependence of some ionospheric ion-neutral reactions from 300–900 K, *J. Geophys. Res.*, **79**(31), 4753–4756.
- Love, S. G., and D. E. Brownlee (1991), Heating and thermal transformation of micrometeoroids entering the Earth's atmosphere, *Icarus*, **89**, 26–43.
- Lübken, F.-J., and M. Rapp (2001), Modelling of particle charging in the polar summer mesosphere: Part 2—Application to measurements, *J. Atmos. Sol. Terr. Phys.*, **63**, 771–780.
- Mason, E. A., and E. W. McDaniel (1988), *Transport Properties of Ions in Gases*, Wiley, London, U. K.
- McIntosh, B. A., and A. Hajduk (1977), Sunrise effect on persistent radar echoes from sporadic meteors, *B. Astron. I. Czech.*, **28**, 280–285.
- McKinley, D. W. R. (1961), *Meteor Science and Engineering*, McGraw-Hill, New York.
- Meek, C. E., A. H. Manson, W. K. Hocking, and J. R. Drummond (2013), Eureka, 80 N, SKIYMET meteor radar temperatures compared with Aura MLS values, *Ann. Geophys.*, **31**, 1267–1277, doi:10.5194/angeo-31-1267-2013.
- Megner, L., M. Rapp, and J. Gumbel (2006), Distribution of meteoric smoke—Sensitivity to microphysical properties and atmospheric conditions, *Atmos. Chem. Phys.*, **6**, 4415–4426.
- Mlynarczyk, M. G., et al. (2013), Atomic oxygen in the mesosphere and lower thermosphere derived from SABER: Algorithm theoretical basis and measurement uncertainty, *J. Geophys. Res. Atmos.*, **118**, 5724–5735, doi:10.1002/jgrd.50401.
- Pack, J. L., and A. V. Phelps (1971), Hydration of oxygen negative ions, *Bull. Am. Phys. Soc.*, **16**, 214.
- Payzant, J. D., and P. Kebarle (1972), Kinetics of reactions leading to O (HO) in moist oxygen, *J. Chem. Phys.*, **56**, 3482.

- Plane, J. M. C. (2012), Cosmic dust in the Earth's atmosphere, *Chem. Soc. Rev.*, *41*, 6507–6518, doi:10.1039/c2cs35132c.
- Plane, J. M. C., and C. L. Whalley (2012), A new model for magnesium chemistry in the upper atmosphere, *J. Phys. Chem. A*, *116*, 6240–6252, doi:10.1021/jp211526h.
- Rapp, M. (2000), Capture rates of electrons and positive ions by mesospheric aerosol particles, *J. Aerosol Sci.*, *31*, 1367–1369.
- Reid, I. M., D. A. Holdsworth, R. J. Morris, D. J. Murphy, and R. A. Vincent (2006), Meteor observations using the Davis mesosphere-stratosphere-troposphere radar, *J. Geophys. Res.*, *111*, A05305, doi:10.1029/2005JA011443.
- Rogers, L. A., K. A. Hill, and R. L. Hawkes (2005), Mass loss due to sputtering and thermal processes in meteoroid ablation, *Planet. Space Sci.*, *53*, 1341–1354.
- Rutherford, J. A., R. F. Mathis, B. R. Turner, and D. A. Vroom (1971), Formation of magnesium ions by charge transfer, *J. Chem. Phys.*, *55*, 3785–3793.
- Shimamori, H., and Y. Hatano (1977), Thermal electron attachment to O_2 in the presence of various compounds as studied by a microwave cavity technique combined with pulse radiolysis, *Chem. Phys.*, *21*, 187–201.
- Singer, W., R. Latteck, L. F. Millan, N. J. Mitchell, and J. Fiedler (2008), Radar backscatter from underdense meteors and diffusion rates, *Earth Moon Planets*, *102*, 403–409.
- Smith, A. K., et al. (2013), Satellite observations of ozone in the upper mesosphere, *J. Geophys. Res. Atmos.*, *118*, 5803–5821, doi:10.1002/jgrd.50445.
- Swider, W. (1969), Processes for meteoric elements in the E-region, *Planet. Space Sci.*, *17*, 1233–1246.
- Tsutsumi, M., T. Tsuda, T. Nakamura, and S. Fukao (1994), Temperature fluctuations near the mesopause inferred from meteor observations with the middle and upper atmosphere radar, *Radio Sci.*, *29*, 599–610.
- Walls, F. L., and G. H. Dunn (1974), Measurement of total cross sections for electron recombination with NO^+ and O_2^+ using ion storage techniques, *J. Geophys. Res.*, *79*(13), 1911–1915.
- Waters, J. W., et al. (2006), The Earth observing system microwave limb sounder (EOS MLS) on the aura Satellite, *EEE Trans. Geosci. Remote Sens.*, *44*(5), 1075–1092, doi:10.1109/TGRS.2006.873771.
- Whalley, C. L., and J. M. C. Plane (2010), Meteoric ion layers in the Martian atmosphere, *Faraday Discuss.*, *147*, 349–368, doi:10.1039/c003726e.
- Whalley, C. L., J. C. Gomez Martin, T. G. Wright, and J. M. C. Plane (2011), A kinetic study of Mg^+ and Mg-containing ions reacting with O_3 , O_2 , N_2 , CO_2 , N_2O and H_2O : Implications for magnesium ion chemistry in the upper atmosphere, *Phys. Chem. Chem. Phys.*, *13*, 6352–6364, doi:10.1039/c0cp02637a.
- Woo, S. B., L. M. Branscomb, and E. C. Beaty (1969), Sunlight photodetachment rate of ground state O_2^- , *J. Geophys. Res.*, *74*, 2933–2940.
- Younger, J. P., I. M. Reid, R. A. Vincent, and D. A. Holdsworth (2008), Modeling and observing the effect of aerosols on meteor radar measurements of the atmosphere, *Geophys. Res. Lett.*, *35*, L15812, doi:10.1029/2008GL033763.
- Younger, J. P., I. M. Reid, and R. A. Vincent (2013), The diffusion of multiple ionic species in meteor trails, *J. Atmos. Sol. Terr. Phys.*, *118*, 119–123, doi:10.1016/j.jastp.2013.10.007.